WP14ER-PR(18) 21313

P Paruta et al.

Blob velocity scaling in diverted tokamaks: a comparison between theory and simulation

Preprint of Paper to be submitted for publication in
Physics of Plasmas

This work has been carried out within the framework of the EUROfusion Consortium and has received funding from the Euratom research and training programme 2014-2018 under grant agreement No 633053. The views and opinions expressed herein do not necessarily reflect those of the European Commission.

Blob velocity scaling in diverted tokamaks: a comparison between theory and simulation

Paola Paruta[1], C. Beadle[1], P. Ricci[1], and C. Theiler[1]

[1]Ecole Polytechnique Fédérale de Lausanne (EPFL), Swiss Plasma Center (SPC), CH-1015 Lausanne, Switzerland

November 10, 2018

Abstract

The present work uses the results of a fluid full-turbulence 3D simulation of the tokamak periphery to present the first self-consistent analysis of the radial velocity scaling of plasma blobs in a diverted geometry. A diverted double-null configuration is considered, and the blob motion is studied using a pattern recognition algorithm. The velocity obtained from the simulation results is compared to an analytical scaling accounting for the presence of the X-point. Agreement is found between numerical and analytical results.

1 Introduction

The dynamics in the periphery of magnetic fusion devices is characterised by the presence of blobs. These are coherent structures of enhanced plasma density with respect to the background, spatially localised in the plane perpendicular to the magnetic field and elongated in the parallel direction [1]. Because of their shape, blobs are also known as filaments. Blobs detach from the main plasma and move radially outwards, making turbulence at the edge of fusion devices intermittent and significantly contributing to the radial transport mechanisms in the SOL. Blobs have been observed in tokamaks (e.g., in the Caltech Research Tokamak [2], Alcator C-Mod [3], JET [4], JT-60U [5], Tore Supra [6], TCV [7]), stallarators (e.g., in the W7-AS stellarator [8], and in TJ-K [9]), reversed field pinches [10], and basic plasma devices (e.g. in LAPD [11] and in TORPEX [12]). They can lead to enhanced intermittent heat flux on the main vessel wall, possibly damaging radio frequencies antennas, wall tiles, and causing sputtering of impurities [13], [14], [15].

It is generally believed that blobs are the result of the non-linear saturation of interchange-like instabilities in the edge, with the density fluctuation sheared apart by the $\mathbf{E}\times\mathbf{B}$ velocity and detached from the main plasma, as observed in JET [16] and in TORPEX [12], and as described by 2D fluid models, e.g. [17]. Once detached from the main plasma, blobs move radially outwards. An extensive review of the literature on blob motion can be found in Ref. [1]. The radial motion results from the vertical charge separation inside the blob stemming from the effect of the magnetic gradient and curvature drifts. The charge separation leads to an electric field and its associated $\mathbf{E}\times\mathbf{B}$ drift that causes the blob to move radially outwards. This basic mechanism of radial motion is confirmed by a series of blob studies conducted on the TORPEX device [18], [19], by experiments in limited and diverted plasmas on TCV [20],

and by numerical simulations of seeded blobs (see, e.g., [21], [22], [23], [24]). Considering a self-consistent simulation of a TCV discharge in limited configuration, in [25] a pattern-recognition algorithm for blob tracking showed good agreement of the blob velocity with the theoretical scalings.

In the present work we investigate for the first time the velocity scaling of blob self-consistently generated in a simulation of SOL plamsa turbulence in diverted configuration. In previous studies, the effect of the X-point on blob motion has been investigated using simulations of a single seeded blob [26], for this purpose with the BOUT++ code [27] was used, to reproduce the experimental work of [19] on TORPEX. In addition, the magnetic shear effect of blobs has been studied as a proxy for the X-point in Refs. [28] and [29]. Only very recently the study of blob motion has been approached by using 3D full-turbulent self-consistent simulations in diverted configuration. Results of a full 3D turbulent simulation with the XGC1 gyrokinetic code of a DIII-D H-mode discharge have been used to carry out an initial investigation of the blob properties [30]. In the present work, we extend the use of the pattern recognition algorithm introduced in [25] to analyse the blob motion in a full SOL turbulent simulation in double-null configuration. The simulation is carried out with the GBS code. GBS [31], [32], [33] is a 3D code that simulates the plasma turbulent dynamics in the tokamak periphery by evolving the two-fluid drift reduced Braginskii's equations [34]-[35]. In the past years GBS has helped investigating plasma dynamics in limited tokamaks, for example, by providing predictions of the SOL width [36]. Recently GBS capabilities have been extended to the simulation of diverted scenarios [33], by abandoning the use of flux coordinates, that present a singularity at the X-point.

The results from a GBS simulation in diverted double-null configuration are here compared with a theoretical scaling developed to predict blob velocity in the presence of an X-point ([37]). As pointed out also by a recent experimental work on ASDEX Upgrade [38] and in simulations [39], collisionality can affect the blob velocity scaling. Our results focus on the high collisionality regime and, depending on the blob size, we identify the polarization current or the parallel current as balance mechanisms to the interchange drive. Our simulations results are in good agreement with the theoretical scalings.

This paper is organised as follows. Leveraging previous derivations by Myra *et al.* [37], we provide the analytical scaling to estimate the velocity of blobs in diverted configurations in Sec. 2. Then, Sec. 3 presents the GBS simulation results obtained in double-null configuration. Blobs are detected and tracked to determine their velocity, size, and collisionality, by using the blob tracking technique presented in Sec. 4. Finally, the simulation results of the blob radial velocity are compared with the analytical scaling in Sec. 5. Conclusions follow.

2 Blob velocity analytical scaling in the presence of an X-point

Analytical predictions of the blob radial velocity can be obtained by using simplified 2D two-fluid models, describing the plasma dynamics in the plane perpendicular to the magnetic field. These models usually consider continuity equation, charge conservation, and a closure for the parallel current. Examples can be found Refs. in [40], [13], [18]. The most investigated of such analytical 2D models to account for the effect of an X-point on blob transport, is the two-region model [37]. The two-region model separates the upstream and the divertor regions, labelled as region 1 and 2, respectively (see Fig. 1). In the upstream region, the unfavourable curvature of the magnetic field leads to the formation of an electric dipole that

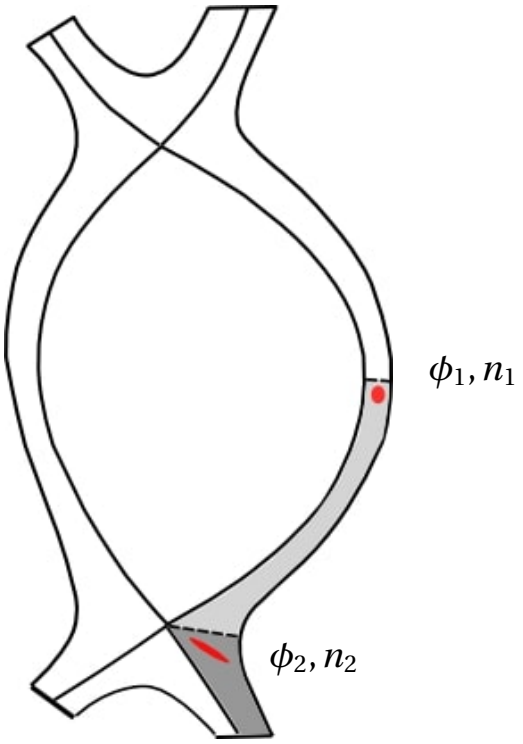

Figure 1: Schematic illustration of the two region model. Region 1 (light gray) correspond to the outboard low field side, where the curvature drive β is active, and extend from midplane to the X-point region. Here the flux expansion is maximal and causes the blobs to elongate and tilt due to field line mapping, disconnecting region 1 from the divertor, i.e. region 2 in darker gray, characterised by the current to the sheath.

provides most of the drive for the blob radial motion. In the divertor region, the magnetic flux expansion causes the blob to elongate in one direction and squeeze in the other (to guarantee mass conservation). The stretching of the blob facilitates the damping of the blob charge separation by cross-field currents.

By following the calculation in Ref. [37], we retain the corrections due to blob density, blob ellipticity, and magnetic field line length difference between the two regions in the evaluation of the blob velocity. We derive the two-region model in the Appendix. In this section, we present the final results of our calculation and leave the details to the Appendix.
The two-region model allows the identification of four different blob motion regimes [37], which correspond to four different mechanisms to balance the curvature drive in region 1. In the sheath connected regime, denoted as C_s, the curvature drive is balanced by the current flowing to the sheath. In the ideal interchange mode regime, C_i, the ion polarisation current in region 2, due to the fanning of the flux surfaces, balances the drive. In the resistive ballooning regime, RB, the ion polarisation current in region 1 dominates. Finally, in the resistive X-point regime, RX, the parallel current flowing between the two regions is the key damping mechanism. Each regime is characterised by a different blob velocity to size scaling.

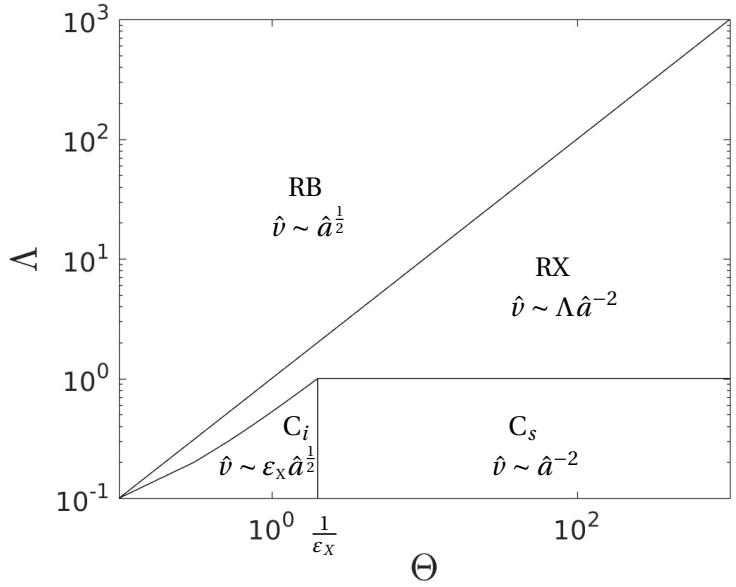

Figure 2: Characterisation of blob regimes in the (Λ, Θ) plane and correspondent velocity to size scaling, as derived in [37] from the two region model.

We find that the regimes are defined by the values of the following parameters:

$$\Lambda = \frac{\nu^{e/i} L_1^2}{\rho_s \Omega_e L_2} \tag{1}$$

$$\Theta = \hat{a}^{\frac{5}{2}} = \left(\frac{a_b}{a^*}\right)^{\frac{5}{2}} \tag{2}$$

The collisionality parameter Λ in eq. (1) can be interpreted as the ratio between the resistivity in region 1 and the sheath resistivity. If Λ is high, region 1 is decoupled from the sheath. In eq. (1), $\nu_1^{e/i}$ is the electron to ion collision frequency in region 1, present in Ohm's law, while $\rho_s = \sqrt{T_e/m_i}/\Omega_i$ is the ion sound gyro-radius. The electron gyro-frequency Ω_e is defined as $\Omega_e = eB/m_e$ (e is the electron charge, m_e the electron mass, and B the magnetic field strength at the blob location in region 1). We note that the two-region model is derived in the isothermal limit, hence T_e at the target is considered to be the same as T_e in region 1, with no distinction between blob and background temperature. In eq. (1) the parallel lengths of the magnetic field line in regions 1 and 2 are L_1 and L_2, respectively.
The parameter Θ and blob normalised size $\hat{a}$ in eq. (2) are given by the ratio between the physical blob size a_b and the reference size a^*. The expressions in physical units for the blob size a_b and the reference size a^* as derived in Appendix (removing the large aspect ratio approximation), are:

$$a_b = \left(\frac{2a_y}{\pi}\right)^{\frac{4}{5}} a_x^{\frac{1}{5}} \tag{3}$$

$$a^* = \rho_s \left(\frac{2L_2^2}{\rho_s R}\right)^{\frac{1}{5}} \left[\frac{\Delta_x n_1}{n_{0,1}}\right]^{\frac{1}{5}} \tag{4}$$

With respect to Myra *et al.* [37], eq. (3) provides an expression for a_b, that differentiate the radial (or poloidal) blob size a_x (or a_y). More precisely, the radial direction x is, the $\nabla\psi$ direction orthogonal to the flux surfaces and y indicates the binormal direction orthogonal to both $\nabla\psi$ and magnetic field versor $\mathbf{b}$. The term within square brackets in eq. (4), not appearing in [37], accounts for the effect of blob density and blob ellipticity. The parameter $n_{0,1}$ in eqs. (4)-(6) corresponds to the mean between the maximal blob density value at midplane and the background equilibrium density value. $\Delta_X n_1$ and a_x are introduced to approximate the density gradient in the radial direction as a ratio between a density difference and a radial length, i.e. $\partial_x n_1 \sim \Delta_x n_1 / a_x$. Ref. [37] introduced a practical way to visualise the four regimes in terms of Λ and Θ, as well as their transition thresholds (see Fig. 2). Each regime presents a different velocity scaling in terms of the normalised velocity:

$$\hat{v} = \frac{v_x}{v^*} \tag{5}$$

with

$$v^* = c_{s,1}\left(\frac{\rho_s^2 L_2}{R^3}\right)^{\frac{1}{5}}\left[8\frac{(\delta n_1)^5}{(\Delta_x n_1)^2 n_{0,1}^3}\left(\frac{\pi a_x}{2a_y}\right)^2\right]^{\frac{1}{5}} \tag{6}$$

Here δn_1 is the amplitude of the density fluctuation above $n_{0,1}$ and a_y is the Half Width Half Maximum (HWHM) blob poloidal size, i.e. half of the poloidal blob size measured half way between the blob density maximum and the background density value (corresponding to the $n_{0,1}$ threshold). The major radius R has to be taken at the blob location in region 1, around midplane, as it results from approximating the magnetic field curvature at the origin of the drive in region 1.

3 GBS simulation in double-null configuration

The present section presents the physical model behind the GBS code, as well as the results of a simulation run in double-null configuration which will be used for our study. GBS implements a two-fluid model based on the drift-reduced Braginskii's set of equations [35]. The interaction between plasma and wall is described by the magnetic pre-sheath boundary conditions [41]. The code uses toroidal coordinates to allow for the simulation of diverted configurations. Ref. [33] reports on the implementation and verification of the version of GBS used for the present study.

3.1 Physical model

Zeiler *et al.* [35] drift-reduced approximation of the Braginskii's equations [34] relies on the assumption that turbulence in the periphery of a tokamak device occurs on a time scale considerably longer than the gyro-motion ($\partial_t \ll \Omega_i = eB/(m_i c)$) and on a length scale larger than the ion gyro-radius ρ_i. As a result, the velocity perpendicular to the magnetic field line can be described as the sums of the $\mathbf{E}\times\mathbf{B}$, diamagnetic velocity, and ion-polarisation drifts. The cold-ion version of the drift-reduced Braginskii's set of equations used for this work can be

written as

$$\frac{\partial n}{\partial t} = -\frac{\rho_\star^{-1}}{B}[\phi, n] + \frac{2}{B}\left[C(p_e) - nC(\phi)\right] - \nabla_\parallel(n v_{\parallel e}) + S_n + D_n \nabla_\perp^2 n \tag{7}$$

$$\frac{\partial v_{\parallel e}}{\partial t} = -\frac{\rho_\star^{-1}}{B}[\phi, v_{\parallel e}] - v_{\parallel e}\nabla_\parallel v_{\parallel e} + \frac{m_i}{m_e}\left(\nu J_\parallel + \nabla_\parallel \phi - \frac{1}{n}\nabla_\parallel p_e - 0.71\nabla_\parallel T_e\right) \tag{8}$$
$$+\frac{4}{3n}\frac{m_i}{m_e}\eta_{0,e}\nabla_\parallel^2 v_{\parallel e} + D_{v_{\parallel e}}\nabla_\perp^2 v_{\parallel e}$$

$$\frac{\partial v_{\parallel i}}{\partial t} = -\frac{\rho_\star^{-1}}{B}[\phi, v_{\parallel i}] - v_{\parallel i}\nabla_\parallel v_{\parallel i} - \frac{1}{n}\nabla_\parallel(p_e) + \frac{4}{3n}\eta_{0,i}\nabla_\parallel^2 v_{\parallel i} + D_{v_{\parallel i}}\nabla_\perp^2 v_{\parallel i} \tag{9}$$

$$\frac{\partial T_e}{\partial t} = -\frac{\rho_\star^{-1}}{B}[\phi, T_e] - v_{\parallel e}\nabla_\parallel T_e + \frac{4}{3}\frac{T_e}{B}\left[\frac{1}{n}C(p_e) + \frac{5}{2}C(T_e) - C(\phi)\right] \tag{10}$$
$$+\frac{2}{3}T_e\left[0.71\nabla_\parallel v_{\parallel i} - 1.71\nabla_\parallel v_{\parallel e} + 0.71(v_{\parallel i} - v_{\parallel e})\frac{\nabla_\parallel n}{n}\right]$$
$$+S_{T_e} + \chi_{\perp,e}\nabla_\perp^2 T_e + \chi_{\parallel,e}\nabla_\parallel^2 T_e$$

$$\frac{\partial \omega}{\partial t} = -\frac{\rho_\star^{-1}}{B}[\phi, \omega] - v_{\parallel i}\nabla_\parallel \omega + \frac{B^2}{n}\nabla_\parallel J_\parallel + \frac{2B}{n}C(p_e) + D_\omega \nabla_\perp^2 \omega \tag{11}$$

$$\nabla_\perp^2 \phi = \omega \tag{12}$$

In eqs. (7)-(12) all variables are dimensionless and, in the following, we use a tilde to denote physical variables, unless specified otherwise. We define the plasma density $n = \tilde{n}/n_0$, the electron temperature $T_e = \tilde{T}_e/T_{e0}$, the electrostatic potential $\phi = e\tilde{\phi}/T_{e0}$, the electron parallel velocity $v_{\parallel e} = \tilde{v}_{\parallel e}/c_{s0}$, the ion parallel velocity $v_{\parallel i} = \tilde{v}_{\parallel i}/c_{s0}$ and the vorticity $\omega = \tilde{\omega}\ e\rho_{s0}^2/T_{e0}$ with n_0, T_{e0}, $c_{s0} = \sqrt{T_{e0}/m_i}$ and $\rho_{s0} = c_{s0}/\Omega_{ci}$ reference density, temperatures, sound velocity and ion sonic Larmor radius expressed in physical units. Time is defined as $t = \tilde{t}\ c_{s0}/R_0$, where R_0 is the major radius at magnetic axis, in physical units. The electron pressure is $p_e = nT_e$. The current is $J_\parallel = n(v_{\parallel i} - v_{\parallel e})$. In our simulation, the values of the dimensionless parameters appearing in Eqs. (7)-(11) are: $\rho_* = \rho_{s0}/R_0 = 1/500$ (normalised ion sonic Larmor radius), $\nu = en_0R_0/(m_i c_{s0}\sigma_i) = 1$ (normalised Spitzer resistivity), $\eta_{0,e} = 5e-3$, $\eta_{0,e,i} = 1$, $\chi_{\parallel e} = 1$ and $\chi_{\perp,e} = 2$. To reduce the computational cost of the simulation we use $m_i/m_e = 200$. The minor radius is $a = 127\rho_{s0}$. Additionally, small numerical diffusion terms of the type $D_f\nabla_\perp^2 f$ are added for numerical stability (in this simulation $D_f = 2$ for all fields). In the density and temperature equations S_n and S_{T_e} denote source terms that mimic the outflow of plasma and heat from the core.

The dimensionless spatial operators appearing in Eqs. (7)-(12) are the parallel gradient $\nabla_\parallel f = R_0\mathbf{b}\cdot\tilde{\nabla}f$, the parallel diffusion operator $\nabla_\parallel^2 f = \nabla_\parallel(\nabla_\parallel f)$, the Poisson brackets $[\phi, f] = \rho_{s0}^2\mathbf{b}\cdot(\tilde{\nabla}\phi\times\tilde{\nabla}f)$, the curvature operator $C(f) = R_0\rho_{s0}\tilde{B}/2(\tilde{\nabla}\times(\mathbf{b}/\tilde{B}))\cdot\tilde{\nabla}$, and the perpendicular diffusion operator $\nabla_\perp^2 = \rho_{s0}^2\tilde{\nabla}\cdot((\mathbf{b}\times\tilde{\nabla}f)\times\mathbf{b})$. Here, f indicates one of the dimensionless fluid quantities $(n, T_{e,i}, v_{\parallel e,i}, \omega, \phi)$ while $\tilde{B}$ and $\mathbf{b} = \tilde{\mathbf{B}}/\tilde{B}$ are the norm and the versor of the magnetic field. In (r,θ,φ) toroidal coordinates we assume an axisymmetric magnetic field of the form:

$$\tilde{\mathbf{B}} = R_0B_0\nabla\varphi + \nabla\varphi\times\nabla\tilde{\psi}(\tilde{r},\theta) \tag{13}$$

with B_0 magnetic field at the magnetic axis, $\tilde{\psi}$ magnetic poloidal flux. Under the assumption of small inverse aspect ratio $\varepsilon = a/R_0$ and large safety factor q, and using eq. (13), the

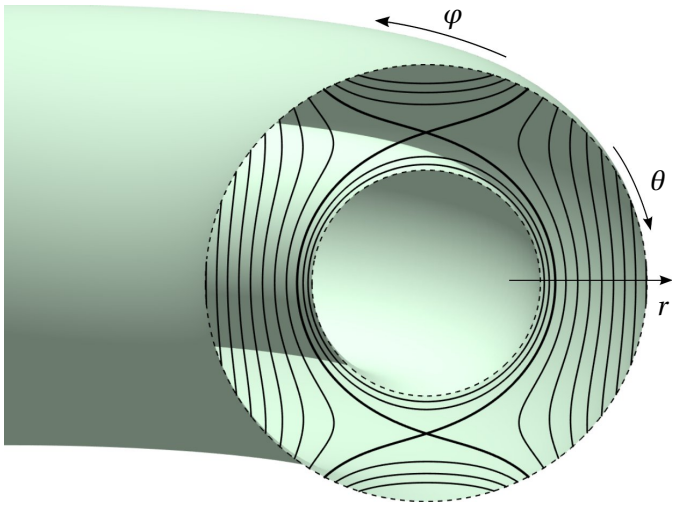

Figure 3: Visualisation of GBS computational domain and toroidal coordinates (r,θ,φ) used to implement the double-null configuration in eq. (18).

differential operator expressions in (r,θ,φ) toroidal coordinates are:

$$\nabla_\parallel f = \frac{B_0}{|B_0|}\frac{\partial f}{\partial \varphi} + \frac{a}{\rho_{s0}}\partial_{\hat{r}}\psi\frac{1}{r}\frac{\partial f}{\partial \theta} - \frac{a}{\rho_{s0}}\frac{1}{\hat{r}}\partial_\theta\psi\frac{\partial f}{\partial r} \tag{14}$$

$$[\phi, f] = \frac{1}{r}\frac{B_0}{|B_0|}[\phi, f]_{r,\theta} \tag{15}$$

$$C(f) = \frac{B_0}{|B_0|}\left(\sin\theta\frac{\partial f}{\partial r} + \frac{\cos\theta}{r}\frac{\partial f}{\partial \theta}\right) \tag{16}$$

$$\nabla_\perp^2 f = \frac{\partial^2 f}{\partial r^2} + \frac{1}{r^2}\frac{\partial^2 f}{\partial \theta^2} \tag{17}$$

where two different dimensionless form of the radial coordinate appear: $\hat{r} = \tilde{r}/a$ is used in relation to ψ derivatives, and $r = \tilde{r}/\rho_{s0}$ in relation to f derivatives. The dimensionless poloidal flux ψ is defined as $\psi = \tilde{\psi}/(a^2 B_0)$. The details of the derivation of the differential operators can be found in Ref. [33]. Since the physical model in Eqs. (7)-(12) considers the electrostatic case, the equilibrium magnetic field is unperturbed throughout the simulation and $\partial_{\hat{r}}\psi$, $\partial_\theta\psi/\hat{r}$ are given as input to the simulation. For this study ψ is chosen to describe a double-null configuration:

$$\begin{aligned}\psi(\hat{r},\theta) = S(\log(\hat{r}-c) &+ \frac{1}{2}I\log((\hat{r}-c)^2 + 4 - 4(\hat{r}-c)\sin\theta) \\ &+ \frac{1}{2}I\log((\hat{r}-c)^2 + 4 + 4(\hat{r}-c)\sin\theta))\end{aligned} \tag{18}$$

with $S = 0.03$, $I = 10$, and $c = 0.9$.

The GBS domain corresponds to a torus with a hollow poloidal cross section (as the tokamak core is not simulated), as it is represented in Fig. 3. At the numerical wall $r = r_{\max}$ the magnetic pre-sheath boundary conditions developed by [41] are considered (neglecting cor-

rection terms linked to f derivatives along the wall):

$$
\begin{aligned}
v_{\parallel,i} &= \pm\sqrt{T_e} \\
v_{\parallel,e} &= \pm\sqrt{T_e}\max\{\exp\left(\lambda - \frac{\phi}{T_e}\right), \exp(\lambda)\} \\
\partial_r \phi &= \mp\sqrt{T_e}\,\partial_r v_{\parallel,i} \\
\partial_r n &= \mp\frac{n}{\sqrt{T_e}}\,\partial_r v_{\parallel,i} \\
\omega &= -(\partial_r v_{\parallel,i})^2 \mp \sqrt{T_e}\,\partial_{rr}^2 v_{\parallel,i} \\
\partial_r T_e &= 0
\end{aligned}
\tag{19}
$$

Where $\lambda = 3$. The plus/minus indicates whether the magnetic field points towards (top sign) or out from the wall (bottom sign) and coincides with the sign of B_r,the radial component of **B**. At the wall location where $B_r = 0$ the boundary condition for $v_{\parallel i}$ jumps from $-\sqrt{T_e}$ to $+\sqrt{T_e}$ (or vice-versa), a similar discontinuity arises for $v_{\parallel e}$. A smoothing function is applied in the vicinity of B_r to avoid such discontinuity (see Ref. [33]). At the inner radial boundary, $r = r_{\min}$, we use an *ad hoc* set of boundary conditions, i.e. $\partial_r f = 0$ for all fields f, except for ω and ϕ, for which we impose $\omega = 0$ and $\phi = \lambda T_e$. The presence of the source of plasma and temperature at $r > r_{\min}$ helps decouple the inner *ad hoc* boundary conditions to the edge and SOL dynamics.

We note that a more complete version of the equations implemented in GBS for diverted magnetic configurations is presented in Ref. [33]. The GBS version for limited configuration additionally solves neutral dynamics and can be run without the Boussinesq approximation for the vorticity and with electromagnetic effects [32].
We finally remark that the drift-reduced Braginskii's equations are solved using a numerical scheme based on a fourth order finite difference algorithm with explicit Rounge-Kutta fourth order method for the time stepping [33].

3.2 Simulation results

The simulation is run on a numerical grid $N_r \times N_\theta \times N_\varphi = 156 \times 450 \times 80$, with time step $\Delta t = 2 \times 10^{-5}$.

After an initial transient, the simulation reaches a quasi-steady state where a strong blob activity is present on the low-field side (LFS) of the device, leading to transport of the plasma out-flowing from the tokamak closed flux surface region to the far SOL. Typical snapshots in this turbulent regime for different plasma quantities appearing in the drift-reduced Braginskii's equations are shown in Fig. 4. The density n (top-left plot) peaks in the closed flux surface region, around the plasma source location. The blobs at the equatorial midplane of the LFS present a mushroom shape typical of high collisionality regimes [37]. At the blob locations, fluctuations in the electric potential ϕ (top-right plot) reveal the presence of the dipolar structure responsible for the blob motion. The GBS physical model allows T_e to vary (bottom-left plot in Fig. 4). A temperature difference between blobs and background increases the drive for the blob radial motion through the enhancement of the $C(p_e)$ term in the vorticity equation, and causes the blob to rotate due to $\mathbf{E} \times \mathbf{B}$ drift [13] because $\phi \propto T_e$ in the SOL in the sheath-limited regime. The rotation of the blob dipole can reduce its outwards radial motion. We assume that these effects are negligible (or balance) and use the two-region model,

which is isothermal, to analyse the results. The parallel current $J_\parallel$ in Fig. 4) exhibits turbulent behaviour at the LFS where the blobs are located.

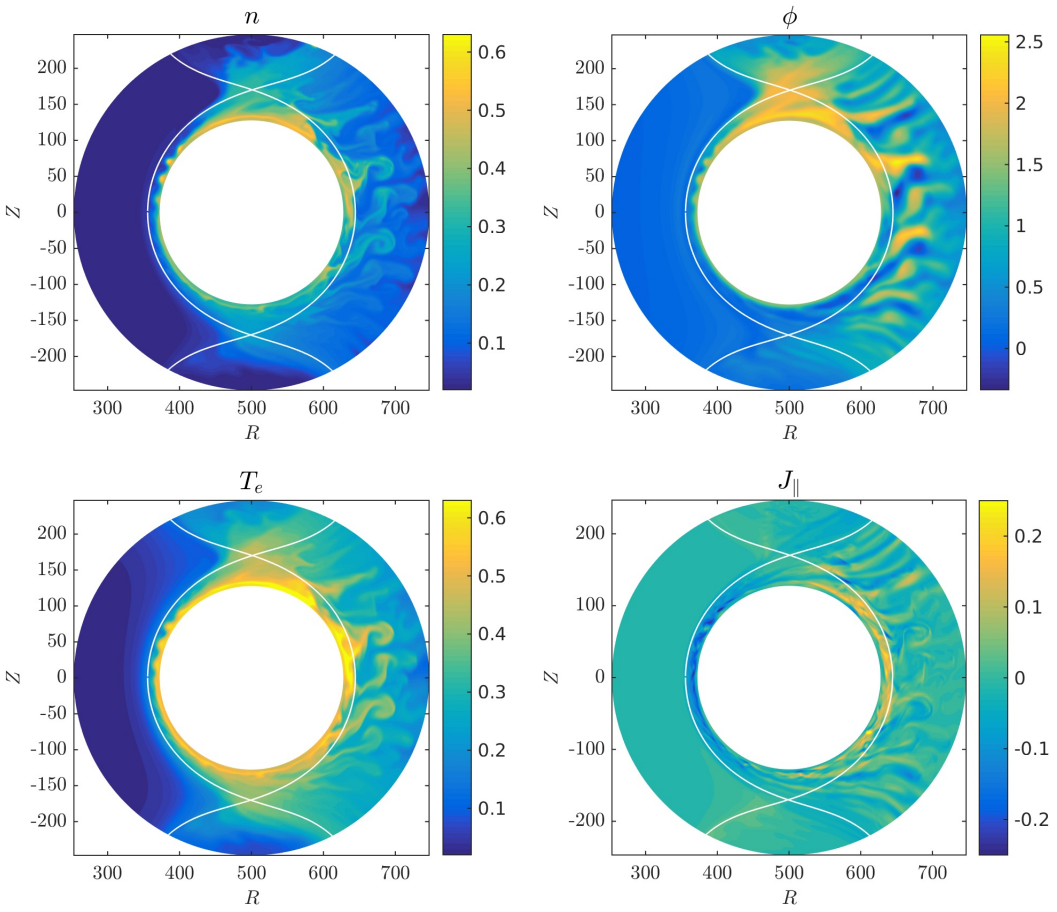

Figure 4: From left to right, top to bottom, typical snapshots of plasma density, electric potential, electron temperature and plasma current, in the GBS double-null simulation considered for our blob analysis (the separatrix is traced by the white line).

4 Blob tracking technique and evaluation of blob parameters

The analysis of blob motion is performed on a time window of 73 R_0/c_{s0} time units during the quasi-steady state. To detect blobs in the GBS simulation we use a pattern recognition algorithm similar to the one presented in Ref. [25]. The analysis is carried out in the poloidal plane since the large inverse aspect ratio and large safety factor assumptions allow us to approximate the plane perpendicular to **b** with the poloidal plane. We define as blob a structure of enhanced density (at least 2.5 times the fluctuation level) that moves coherently (i.e., it exists for $\Delta t > 0.2$). More precisely, blobs are detected from the simulation results as follows. We first identify the regions $\Omega_{b,\text{high}}$ with density larger than the average density, n_{bg}, by 2.5 times the fluctuation level, σ_n, that is:

$$n(r,\theta,t) > n_{bg} + 2.5\sigma_n, \tag{20}$$

We remark that the average background density is computed by time and toroidally averaging the density during the quasi-steady state, $n_{bg}(r,\theta) = \langle n \rangle_{t,\varphi}$, and the standard deviation is defined as $\sigma_n(r,\theta) = \sqrt{\langle (n(r,\theta,\varphi_k,t_m) - n_{bg}(r,\theta))^2 \rangle_{t,\varphi}}$. Once the regions $\Omega_{b,\text{high}}$ where eq. (20) is satisfied are detected, a pattern recognition algorithm groups the points that are connected and therefore belong to and form the same blob. A blob is then tracked from one time frame to the next by checking whether there is spatial overlapping between $\Omega_{b,\text{high}}$ belonging to two subsequent time frames. Splitting and merging of blobs is also allowed by checking if two blobs end up corresponding to one single blob in the following time frame or vice-versa. The blob detection is carried out in one poloidal plane and we analyse only the blobs detected around the outboard midplane. This also avoids counting the same blob twice, when the blob extends over the magnetic field by more than one toroidal turn.

Having detected the blobs, we determine their size and velocity. The algorithm described above is efficient in tracking blobs, but it often underestimates the blob size, as it only detects the high density peak of a blob, which is shown by the striped region in Fig. 9. In order to determine the blob size in a way consistent with the analytical two-region model, one needs to detect the region corresponding to the density fluctuation above the half maximum, n_0. This corresponds to the colored region that we will referred to as Ω_b in Fig. 9. To determine Ω_b, we take an area $\Omega_{b,\text{ext}}$ larger than $\Omega_{b,\text{high}}$ by $\sim 30\rho_{s0}$ in every direction, and re-define the blob as the set of connected (r,θ) points in $\Omega_{b,\text{ext}}$ for which:

$$n(r,\theta,t) > n_0 = n_{bg} + \delta n = n_{bg} + \max_{\Omega_{b,\text{high}}(t)} \frac{n - n_{bg}}{2} \tag{21}$$

We note that the poloidal radius of Ω_b is the half-width half-maximum (HWHM) of the blob density perturbation, corresponding to a_y of the two-region model (see Fig. 9). The blob HWHM is commonly used to indicate the blob size in blob studies [25], [42].

The blob detection algorithm also verifies the presence of sufficient overlapping in the subsequent time frames

$$\frac{||\Omega_b(t_m) \cap \Omega_b(t_{m+1})||}{||\Omega_b(t_m)||} > 0.8 \tag{22}$$

as well as

$$\left| \frac{||\Omega_b(t_m)|| - ||\Omega_b(t_{m+1})||}{||\Omega_b(t_m)||} \right| < 0.2 \tag{23}$$

to assess that the the blob size does not change abruptly. If the blob domain Ω_b changes considerably from one time frame to the next, we consider them as two different blobs. The threshold coefficients 0.8 and 0.2 in the double-null case are chosen so that the blobs have size and shape that are continuous enough, without incurring excessive splitting.

In order to compare the two-region model in Sec. 2 with the simulation results, we estimate a_x, a_y, Λ, $\Theta = \hat{a}^{5/2} = (a_b/a^*)^{5/2}$, and $\hat{v} = v_x/v^*$ from the blob parameter in region 1. We focus on blobs detected in the proximity of the midplane, therefore we require the blob center of mass to be at most $50\rho_{s0}$ away from midplane, $-50 < Z_{CM} < 50$, with the center of mass location (R_{CM}, Z_{CM}) defined as

$$R_{CM} = \frac{\langle R\, n(R,Z) \rangle_{\Omega_b}}{\langle n \rangle_{\Omega_b}}, \qquad Z_{CM} = \frac{\langle Z\, n(R,Z) \rangle_{\Omega_b}}{\langle n \rangle_{\Omega_b}} \tag{24}$$

In the proximity of the midplane x and y directions correspond approximately to the radial and vertical directions, R and Z. Therefore we approximate the blob radii $a_x = a_R$ and $a_y = a_Z$ to correspond to half of the extension of Ω_b along the R and Z directions.
To have a better estimate of the blob size, we use the average between the top 10% of the ΔZ and ΔR values for each blob, where ΔZ (ΔR) is the vertical (radial) extension of the blob area at a given R (Z).

To estimate the quantity $n_{0,1}$ in Eqs. (4) and (6), we take the minimum value of n in Ω_b, as suggested by figure 9, averaging over the lowest 10% density values. To compute the density perturbation $\Delta_x n_1$ that we use to approximate $\partial_x n_1$, we look at the maximal blob density difference along R, for every fixed Z with $(R,Z) \in \Omega_b$, that we denote $\Delta n_b|_Z$ and we take the average of the top 10% values. Analogously, to compute δn_1 in eq. (6) we consider the largest blob density difference along Z. Note that if the background density value is constant in the radial direction (across the blob domain) then $\delta n_1 = \Delta_x n_1$ and the two estimates coincide. Finally, we compute the Larmor radius ρ_s which in GBS dimensionless units corresponds to $\sqrt{T_e}$, using a similar technique to the one used to evaluate $n_{0,1}$.

The radial velocity $v_x = v_R$ (in c_{s0} units) is computed by tracking the radial center of mass location R_{CM} during a blob lifetime:

$$v_R(t_i) = \frac{R_{CM}(t_{i+1}) - R_{CM}(t_i)}{t_{i+1} - t_i} \rho_*^{-1} \tag{25}$$

where t_i is the snapshot time (in the present study $t_{i+1} - t_i = 0.05$).

In the considered double-null configuration the magnetic field line length in the upstream region 1, L_1, is approximately 2/3 of the magnetic field line length from target to the midplane $L_\parallel$ (in the proximity of the LCFS). This can be computed numerically as:

$$L_\parallel = \frac{1}{2}\int dl_\parallel = \frac{1}{2}\int \rho_* \frac{\sqrt{B_{pol}^2 + B_{tor}^2}}{B_{pol}} ds \tag{26}$$

where $B_{tor}^2 = B_\varphi B^\varphi = 1$, $B_{pol}^2 = B_\theta B^\theta + B_r B^r = \varepsilon^2((\partial_{\hat{r}}\psi)^2 + (\partial_\theta \psi/\hat{r})^2)$, with ε being the inverse aspect ratio, and the integral from the lower to the upper strike point is performed along a flux surface.

Finally, we rewrite the expression for Λ, Θ (or $\hat{a}$), and $\hat{v}$, in Eqs. (1)-(5) using quantities appearing in in the drift-reduced Braginskii model (Eqs. (7)-(12)) units, with $x \to R$ and $y \to Z$:

$$\Lambda = \frac{\nu n_1 L_1^2}{L_2 \rho_s} \tag{27}$$

$$\Theta = \hat{a}^{\frac{5}{2}} = \left(\frac{a_b}{a^*}\right)^{\frac{5}{2}} = \left[\frac{\left(\frac{2a_Z}{\pi}\right)^{4/5} a_R^{1/5}}{\left(2\rho_*^{-1}\frac{\Delta_R n_1}{n_{0,1}}\rho_s^4 L_2^2\right)^{1/5}}\right]^{5/2} \tag{28}$$

$$\hat{v} = \frac{v_R}{v^*} = \frac{v_R}{\left(\rho_*^2 \rho_s^7 L_2\right)^{\frac{1}{5}}}\left[8\frac{\delta n_1^5}{\Delta_R n_1^2 n_{0,1}^3}\left(\frac{\pi a_R}{2a_Z}\right)^2\right]^{-1/5} \tag{29}$$

5 Comparison between simulation results and analytical predictions

Figure 5 (left) locates the detected blobs in the (Θ, Λ) plane. The normalised velocity $\hat{v}$ of each blob as a function of its size $\hat{a}$ is shown in Fig. 5 (right). The detected blobs belong to the RB and RX regimes, with the threshold between the two regimes being at $\Theta/\Lambda = 1$. The analytical scalings of the two-region model for the blob velocity in the RB and RX regimes, traced by continuous blue and red lines respectively, are shown to be upper bounds of the measured blob velocities. The $\log(\theta/\Lambda)$ colormap indicates wheather a blob belongs to the RB or to the RX regime (the RB blobs are blue and the RX blobs are red/yellow). The transition in color/regime agrees with the change in velocity trend. We also plot the velocity scaling of the sheath connected, C_s, regime (black dashed line), whose velocity to size trend is $\hat{a}^{-2}$ (see Fig. 5 left), which differs from the RX scaling only by the multiplying factor $\Lambda \sim 10$. In the RX regime, the high collisionality causes the blob to partially disconnect from the sheath and, as a consequence, the blob sustains its self-induced electric field more efficiently, resulting in a faster outwards motion. The simulation results show that the sheath connected scaling significantly underestimates the blob velocity, confirming that the large $\hat{a}$ blobs belong to the RX regime. To our knowledge this is the first time that RX behaviour is observed and studied in blob simulations or experiments.

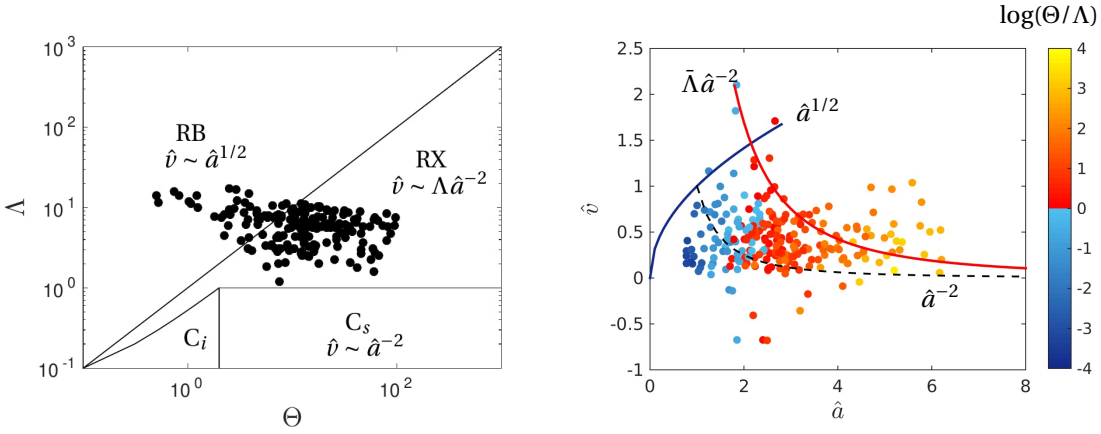

Figure 5: Characterisation of blob regimes in the (Θ, Λ) plane (left panel). The blobs belong to the resistive ballooning (RB) and resistive X (RX) regimes. The normalised blob velocity $\hat{v} = v_Z/v^*$ as a function of the normalised size $\hat{a} = a_b/a^*$ (right panel). Good agreement with the analytical scalings of RB and RX regime (in blue and red solid lines), and very different behaviour with respect to C_s sheath connected regime (in black dashed line) is shown. The color-scheme indicates $\log(\Theta/\Lambda)$, with the transition between the RB and the RX regimes being at $\Theta = \Lambda$.

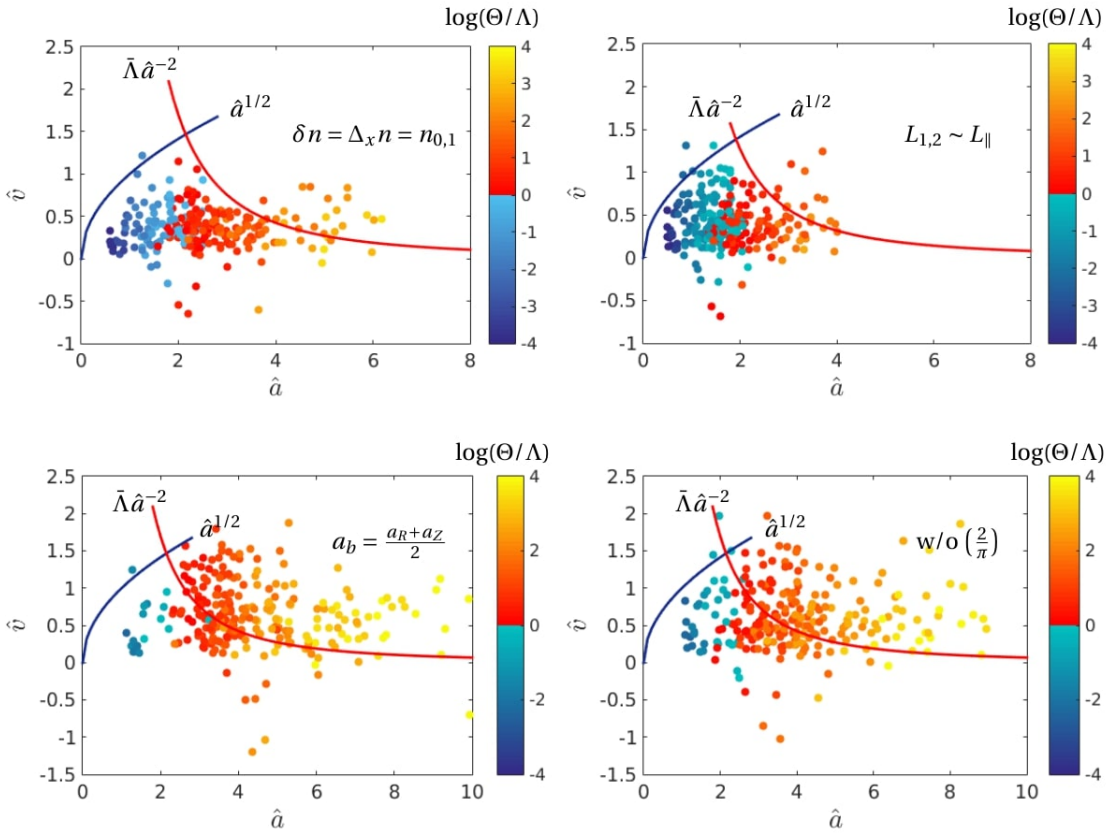

Figure 6: Effect of various approximation of blob scaling. From left to right, top to bottom, impact of: excluding $\delta n/n$ effects, approximating magnetic field line length in region 1 with $L_\parallel = (L_1 + L_2)$, considering a_b to be the average between the radial blob radius a_R and the vertical size a_Z, and removing the $2/\pi$ factor in a_b and v^*. The qualitative behaviour is similar, but quantitatively the agreement with the analytical scaling is worse than in Fig. 5.

The two-region scaling presented in Sec. 2 differs to some extents from the one in Myra *et al.*[37] as it retains density effects, difference between magnetic field line lengths in the upstream and divertor regions, as well as blob ellipticity and the way blob size is measured. In Fig. 6 we test the influence of these effects on the velocity scaling. The top-left panel of Fig. 6 shows that removing the density perturbation effects shifts the blobs distribution to the left and the normalised velocity is reduced. This is due to an increase in both reference size a^* and reference velocity v^*, since we are dropping the terms $(\Delta_x n_1/n_{0,1})^{1/5} < 1$ and $(\delta n_1^5/(\Delta_x n_1^2 n_{0,1}^3))^{1/5} < 1$ in eqs. (4) and (6), respectively. Considering the total magnetic field line length from target to midplane, $L_\parallel$, rather than the field line length in region 1, L_1, (top-right panel of Fig. 6) reduces $\hat{a}$ and impacts the value of Λ, resulting in a slightly worse agreement between the RB/RX regime transition, as indicated by the color code and as suggested by the velocity to size dependence. Finally, taking a_b to be the average between a_R and a_Z instead of eq. (3) (bottom left panel of Fig. 6) significantly impacts the two-region prediction since most blobs are now estimated to belong to the RX regime, with the blobs distribution moving to the right, and the normalised size $\hat{a}$ being overestimated. This is partly due, in this case, to the fact that we drop the $(2/\pi)^{4/5}$ term in a_b, introduced when relating the

wavenumber k_1 in region 1 to a_Z (i.e. $k_1 = 2a_Z/\pi$). Removing the $(2/\pi)^{4/5}$ factor contributes to overestimate the blob size, as shown in the bottom-right panel of Fig. 6.

In Figs. 7 and 8 investigate further the difference between RB blobs and RX blobs by looking at the density, potential and parallel current of typical blobs belonging to the two regimes. Typically, RB blobs are localised closer to the separatrix and they do not extend to the divertor region. On the other hand, RX blobs are localised in the far SOL and develop parallel dynamics, reaching the wall. Nonetheless the associated potential perturbation is relatively small in region 2. A typical blob contoured by a solid black line in the RX regime is shown in Fig. 7. As it can be seen from the top panels, the blob structure extends to the wall and reappears periodically in the poloidal plane, at the locations (identified by red circles) where the magnetic field line that passes through the center-of-mass of the detected blob comes back on the poloidal plane. The blob gets stretched as it approaches the X-points, because of the flux expansion present in these regions. The blob elongation along the magnetic field is also confirmed by the bottom panels that show the plasma density and parallel current on the flux surface of the center-of-mass of the blob in the (s,φ) plane, where s is the poloidal distance from midplane, along the magnetic flux surface of the blob, and φ is the toroidal angle (the square identifies the blob center-of-mass at $\varphi = 0$, which is also shown in the top panels). We remark that the presence of the parallel current in region 1 and region 2 is not negligible. Furthermore, even though the structure can be traced up to the wall, the fluctuations in density and potential decrease moving from midplane to wall, indicating partial disconnection of the blob between the sheath and the midplane.

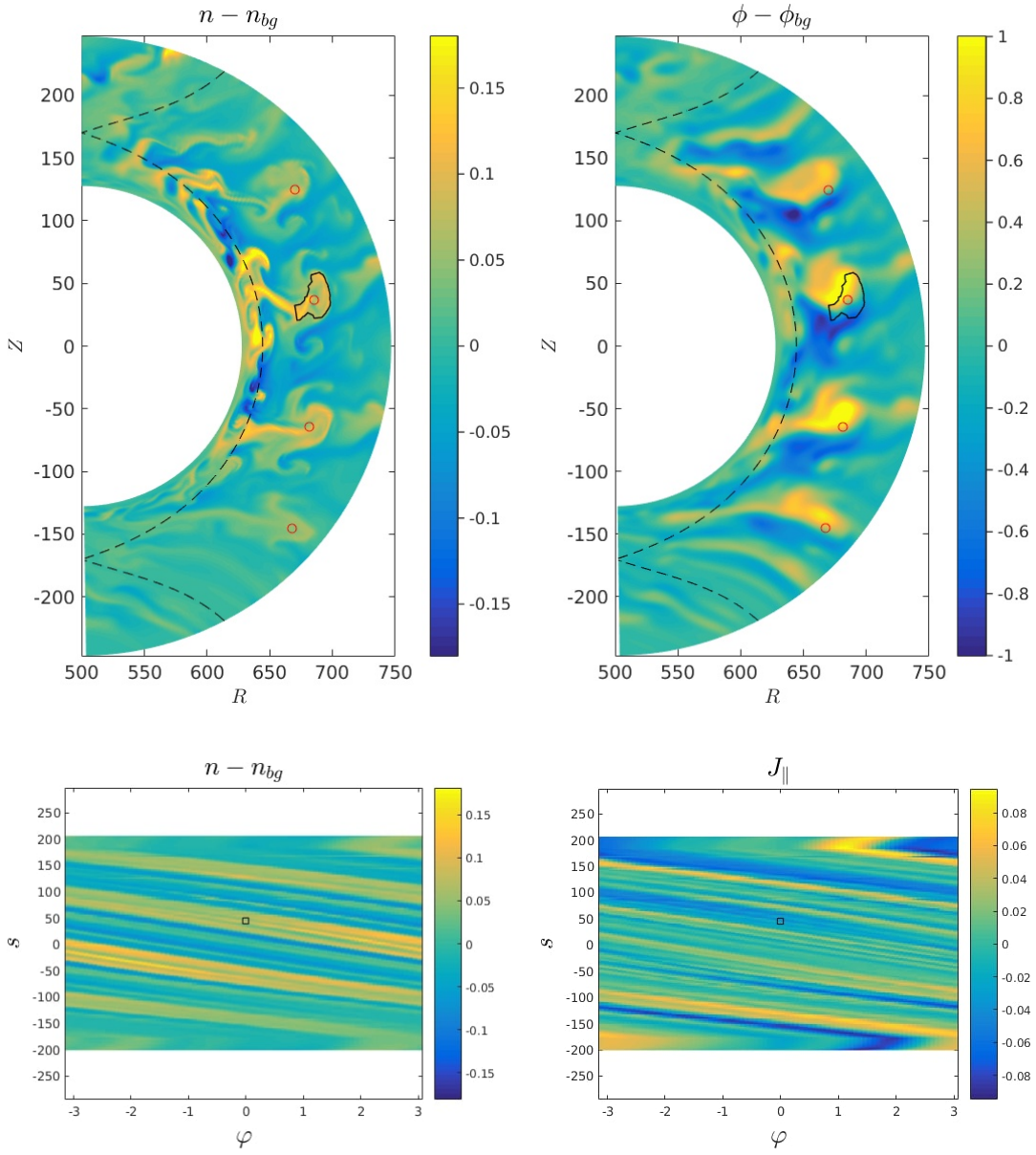

Figure 7: A resistive-X (RX) blob. From left to right, top to bottom: density fluctuation $n - n_{bg}$ in (R, Z), potential fluctuation $\phi - \phi_{bg}$ in (R, Z) (blob perimeter traced with continuous black line), density fluctuation along the flux surface, and parallel current $J_{\parallel} = n(v_{\parallel,i} - v_{\parallel,e})$ along the flux surface (square indicating blob center of mass location). The $\varphi = 0$ poloidal plane represented in the top panels.

Fig. 8 shows the density poloidal snapshot of a RB blob. With respect to the RX blob, it is smaller in size and it is located just outside the separatrix. The electric potential shows the presence of a dipole, which extends outside of the blob perimeter (top right). We note that the blob structure does not reappear periodically on the poloidal plane. Focusing on the flux surface passing through the blob center of mass, we observe that the blob extends along the magnetic field line on the flux surface, without reaching region 2 that starts at $|s| \geq 150$.

Finally, the bottom right plot shows that the parallel current, $J_\parallel = n(v_{\parallel,i} - v_{\parallel,e})$, is almost negligible for a RB blob, in agreement with the model that predicts for a RB blob that the curvature drive is compensated by the perpendicular ion-polarisation current, with the parallel dynamics playing a minor role.

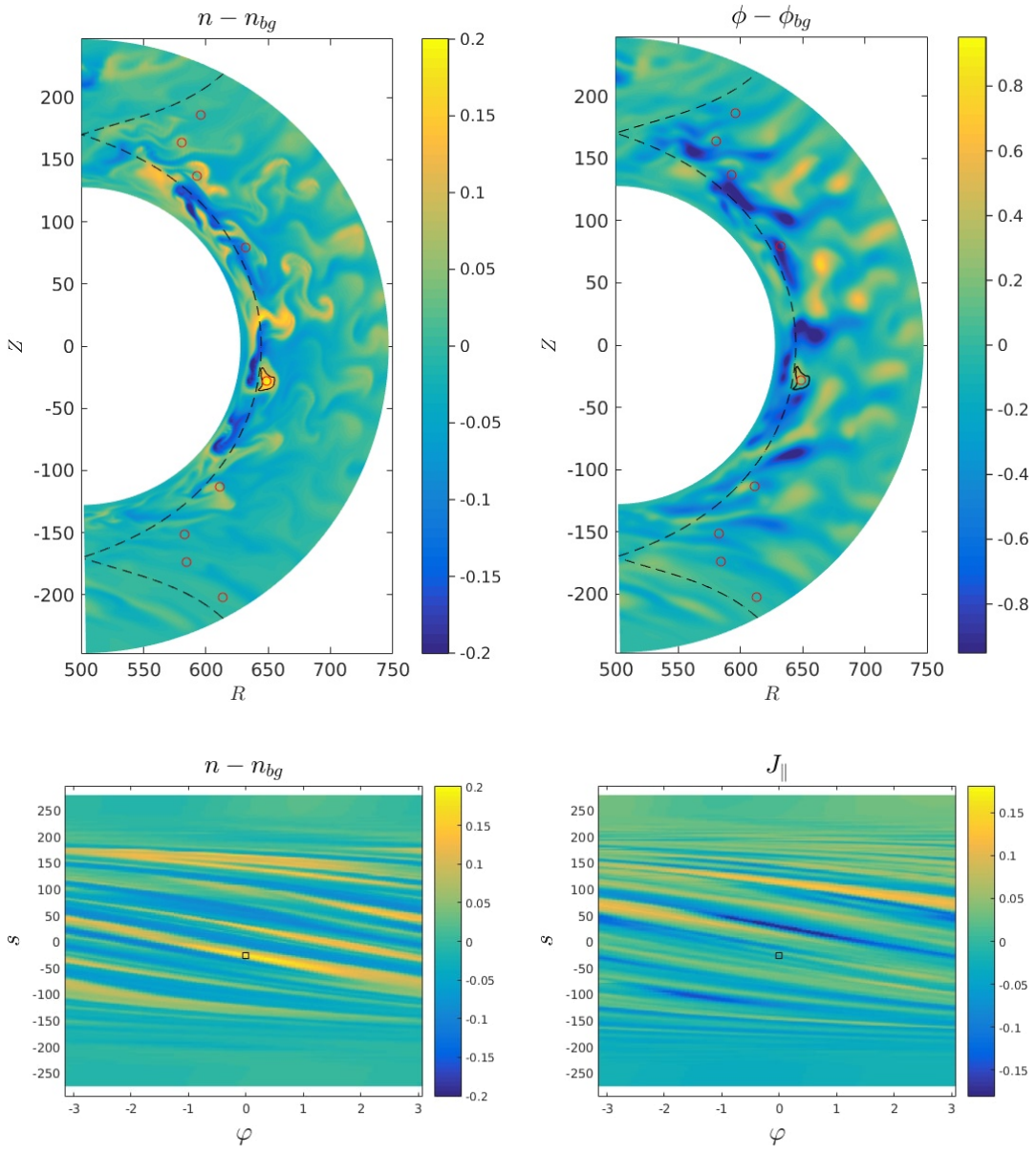

Figure 8: An resistive ballooning RB blob. From left to right, top to bottom: density fluctuation $n - n_{bg}$ in (R, Z), potential fluctuation $\phi - \phi_{bg}$ in (R, Z) (blob perimeter traced with continuous black line), density fluctuation along the flux surface, and parallel current $J_\parallel = n(v_{\parallel,i} - v_{\parallel,e})$ along the flux surface (square indicating blob center of mass location). The $\varphi = 0$ poloidal plane is represented in the top panels.

6 Conclusions

The GBS code is used to investigate blob dynamics in the presence of an X-point. An analytical scaling for the blob velocity as a function of the blob size and plasma collisionality is derived in a diverted geometry following closely the two-region model presented in Ref. [37]. This model accounts for the differences in the physical mechanisms and in the magnetic field geometry that characterise the outboard mid-plane and the divertor regions. The scaling is re-derived starting from a simplified version of the drift-reduced Braginskii's equations for density and vorticity and providing a closure for the parallel dynamics, using Ohm's law and the magnetic pre-sheath physics. The scaling retains the effects of blob plasma density, blob ellipticity, as well as the difference in magnetic field line length in region 1 and 2.
A simulation is run in a double-null configuration, and a blob detection/tracking algorithm is developed and used to compute blob velocity, size and other physical parameters needed to perform a comparison between simulation results and the analytical scaling. The blobs appear to be in the high-collisionality Resistive Ballooning and Resistive X regimes of the two-region model, where the curvature drive is balanced by the perpendicular ion polarisation current and parallel current flow between the two regions, respectively. The analytical scaling constitute an upper bound for the detected blob velocities as a function of their sizes. The effect of blob density and ellipticity are shown to be quantitatively important, although the qualitative trends are unchanged. A detailed analysis of two blobs, one in Resistive X and one in Resistive Ballooning, show density and electric potential fluctuations as well as parallel current profiles that are in agreement with the theoretical expectations. This is the first time that a blob velocity scaling is investigated using full-3D turbulent simulation in diverted geometry.

7 Acknowledgments

We thank Cedric Tsui, James Myra, Federico Nespoli, and Samuel Lanthaler, for the useful discussions. The simulations presented herein were carried out in part at the Swiss National Supercomputing Center (CSCS) under Projects ID s718 and s803 and in part on the CINECA Marconi supercomputer under the GBSSOL project. This work has been carried out within the framework of the EUROfusion Consortium and has received funding from the Fond National Suisse de la Recherche Scientifique and from the Euratom research and training program 2014-2018 under Grant Agreement No. 633053. The views and opinions expressed herein do not necessarily reflect those of the European Commission.

A Re-derivation of the two region model

The drift-reduced Braginskii's equations for density (eq. (7)) and vorticity (eq. (11)) can be simplified around the equatorial midplane as

$$\begin{aligned}
&\frac{\partial \omega_1}{\partial t} + \rho_*^{-1}[\phi_1, \omega_1] = \frac{1}{n_1}\nabla_\parallel J_{\parallel,1} + \frac{2T_e}{n_1} C(n_1) \\
&\frac{\partial n_1}{\partial t_1} + \rho_*^{-1}[\phi_1, n_1] = 0
\end{aligned} \tag{30}$$

and in the divertor region as

$$\frac{\partial \omega_2}{\partial t} + \rho_*^{-1}[\phi_2, \omega_2] = \frac{1}{n_2}\nabla_\parallel J_{\parallel,2}$$
$$\frac{\partial n_2}{\partial t} + \rho_*^{-1}[\phi_2, n_2] = 0 \tag{31}$$

With respect to the drift-reduced Braginskii density equation (eq. (7)), the parallel streaming and magnetic curvature terms are neglected, as they are smaller than the dominant $\mathbf{E}\times\mathbf{B}$ drift. In the vorticity equations, the parallel terms associated with the polarisation current are neglected and, in the divertor region, the interchange drive is also discarded. The large aspect ratio approximation is used, allowing us to drop the normalised magnetic field strength B that appears in [37].

By balancing the divergence of $J_\parallel$ with the resistive term in Ohm's law $J_\parallel = -\nabla_\parallel \phi/\nu$ in the electron velocity equation (8) in the upstream region, we approximate

$$\nabla_\parallel J_{\parallel,1} = \frac{\phi_1 - \phi_2}{\nu L_1^2} \tag{32}$$

where L_1 is length of the magnetic field line from the equatorial midplane to the entrance of the divertor region (normalised to R_0). In the divertor region, a closure for the parallel current can be obtained by integrating $\nabla_\parallel J_\parallel$ along the parallel direction from the interface with the upstream region to the sheath entrance, i.e.

$$\int_2^{sh} \nabla_\parallel J_{\parallel,2}\, dl = J_\parallel\Big|_2^{sh} = -\frac{\phi_1 - \phi_2}{\nu L_1} + \frac{n_2 c_s}{T_e}(\phi_2 - \phi_f) \tag{33}$$

where the sheath current $J_\parallel = n c_s\left(1 - \exp\left(\lambda - \phi/T_e\right)\right)$ is linearised around $\phi \sim \phi_f = \lambda T_e/e$. By applying the current closures and evaluating the curvature terms at the outboard midplane (using eq. (16)), the two-region model becomes:

$$\left(\frac{\partial}{\partial t} + \frac{R_0}{\rho_{s0}}\mathbf{v}_{E,1}\cdot\nabla\right)\nabla_\perp^2\phi_1 = \sigma_1\frac{\phi_1 - \phi_2}{n_1} - \frac{\beta}{n_1}\frac{1}{r}\frac{\partial n_1}{\partial \theta} \tag{34}$$
$$\left(\frac{\partial}{\partial t} + \frac{R_0}{\rho_{s0}}\mathbf{v}_{E,1}\cdot\nabla\right)n_1 = 0 \tag{35}$$
$$\left(\frac{\partial}{\partial t} + \frac{R_0}{\rho_{s0}}\mathbf{v}_{E,2}\cdot\nabla\right)\nabla_\perp^2\phi_2 = -\sigma_2\frac{\phi_1 - \phi_2}{n_2} + \alpha(\phi_2 - \phi_f) \tag{36}$$
$$\left(\frac{\partial}{\partial t} + \frac{R_0}{\rho_{s0}}\mathbf{v}_{E,2}\cdot\nabla\right)n_2 = 0 \tag{37}$$

having defined

$$\sigma_1 = \frac{1}{\nu L_1^2}, \quad \sigma_2 = \frac{1}{\nu L_1 L_2}, \quad \beta = 2\rho_s^2, \quad \alpha = \frac{1}{\rho_s L_2} \tag{38}$$

with L_2 in the magnetic field line length from X-point to wall (in R_0 units). In addition, in Eqs. (34)-(37), the Poisson brackets terms are rewritten as advective terms due to the $\mathbf{E}\times\mathbf{B}$ velocity $\mathbf{v}_E$, for example

$$[\phi, \omega] = \mathbf{b}\cdot\nabla\phi\times\nabla\omega = \mathbf{v}_E\cdot\nabla\omega \tag{39}$$

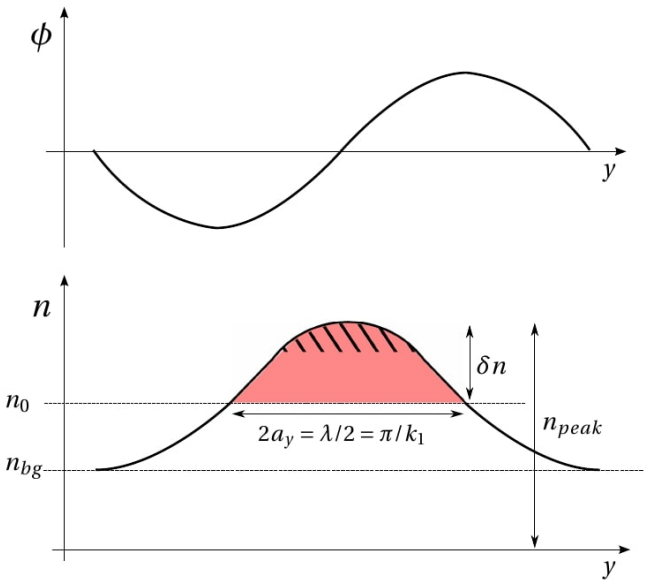

Figure 9: Blob cut along the vertical direction, y, showing potential and density wavelike profiles as expressed in Eqs. (40)-(41) and their relation to the blob density peak n_{peak} and the density background value n_{bg}. We also show the link between wavenumber k_1 and the half width a_y taken at the half maximum location (corresponding to $n = n_0$), i.e. $k_1 = \pi/(2a_y)$.

where $\mathbf{v}_E$ is adimensionalised over c_{s0} and ∇ over ρ_{s0}.

In order to make analytical progress in the analysis of the blob velocity, we linearise the two-region model. We indicate the radial ψ and binormal χ directions ($\mathbf{e}_\chi = \mathbf{b} \times \mathbf{e}_\psi$) with x and y, respectively (they are normalised to ρ_{s0} units) and Fourier decompose $\phi_{1,2}$ and $n_{1,2}$ along the y direction, allowing for different wavenumbers in the two regions, i.e.

$$\phi_1 = \delta\phi_1(x)e^{-i\omega t+ik_1 y}, \qquad n_1 = n_{0,1}(x) + \delta n_1(x)e^{-i\omega t+ik_1 y} \tag{40}$$

$$\phi_2 = \delta\phi_2(x)e^{-i\omega t+ik_2 y}, \qquad n_2 = n_{0,2}(x) + \delta n_2(x)e^{-i\omega t+ik_2 y} \tag{41}$$

The background density is given by $n_{bg} = n_0 - \delta n$ and the peak blob density by $n_{peak} = n_0 + \delta n$ (see Fig. 9). We then approximate $\nabla_\perp^2 \delta\phi_1 \simeq -k_1^2 \delta\phi_1$ (assuming the blob electric potential to vary along the x direction on longer scales than along y, consistently with the physical picture of a dipole generating in y), and we work in the $\mathbf{E} \times \mathbf{B}$ frame of reference, so that the background equilibrium potentials $\phi_{0,1}$ and $\phi_{0,2}$ vanish (assuming they are constant and equal to each other). The linearized two-region model obtained is the following:

$$i\omega k_1^2 \delta\phi_1 = \frac{\sigma_1}{n_{0,1}}\left(\delta\phi_1 - \delta\phi_2\right) - i\beta k_1 \frac{\delta n_1}{n_{0,1}} \tag{42}$$

$$-i\omega\delta n_1 - \rho_*^{-1} i k_1 \delta\phi_1 \frac{\partial n_1}{\partial x} = 0 \tag{43}$$

$$i\omega k_2^2 \delta\phi_2 = \frac{\sigma_2}{n_{0,2}}\left(\delta\phi_2 - \delta\phi_1\right) + \alpha\delta\phi_2 \tag{44}$$

$$-i\omega\delta n_2 - \rho_*^{-1} i k_2 \delta\phi_2 \frac{\partial n_2}{\partial x} = 0 \tag{45}$$

where we made use of Eqs. (39) to write $\mathbf{v}_{E,j}\cdot\nabla \approx -ik_j\delta\phi_j\partial_x$ ($j=1$ and 2). eq. (43) allows us to express δn_1 as a function of $\delta\phi_1$, that is

$$\delta n_1 = -\frac{1}{\omega}\rho_*^{-1}k_1\frac{\partial n_1}{\partial x}\delta\phi_1 \tag{46}$$

Note that the background density can vary in the radial direction, $n_{0,j}=n_{0,j}(x)$ in Eqs. (40)-(41). In the case of uniform background $\partial_x n_j = \partial_x\delta n_j = \delta n_j/a_x$, with a_x half of the radial blob size. eq. (46) can be substituted in eq. (42) to obtain:

$$\omega^2\delta\phi_1 = -i\frac{\sigma_1}{n_{0,1}k_1^2}\omega\left(\delta\phi_1-\delta\phi_2\right)+\frac{\beta}{\rho_*}\frac{1}{n_{0,1}}\frac{\partial n_1}{\partial x}\delta\phi_1 \tag{47}$$

Introducing the characteristic frequencies $\omega_{\sigma,j}=\sigma_j/(n_{0,j}k_1^2)$ and $\gamma_{\rm mhd}^2=-\beta\rho_*\partial_x n_1/n_{0,1}$, this can be written as

$$\omega^2\delta\phi_1 = -i\omega_{\sigma,1}\omega\left(\delta\phi_1-\delta\phi_2\right)-\gamma_{\rm mhd}^2\delta\phi_1 \tag{48}$$

and, using the same notation, eq. (44) becomes

$$\omega\delta\phi_2 = i\omega_{\sigma,2}\frac{k_1^2}{k_2^2}\left(\delta\phi_1-\delta\phi_2\right)-i\omega_{\alpha,2}\delta\phi_2 \tag{49}$$

where $\omega_{\alpha,2}=\alpha/k_2^2$. From Eqs. (48) and (49), the following dispersion relation is derived:

$$\omega^2+\gamma_{\rm mhd}^2+\frac{(i\omega_{\sigma,1}\omega)(\omega+i\omega_{\alpha,2})}{\omega+i\omega_{\sigma,2}k_1^2/k_2^2+i\omega_{\alpha,2}}=0 \tag{50}$$

Since we can approximate $k_2=k_1/\varepsilon_\chi$, with ε_χ inversely proportional to the flux tube fanning, eq. (50) becomes

$$\omega^2+\gamma_{\rm mhd}^2+\frac{(i\omega_{\sigma,1}\omega)(\omega+i\varepsilon_\chi^2\omega_{\alpha,1})}{\omega+i\varepsilon_\chi^2\omega_{\sigma,2}+i\varepsilon_\chi^2\omega_{\alpha,1}}=0 \tag{51}$$

In table 1 we compare the characteristic frequencies, $\gamma_{\rm mhd}$,$\omega_{\sigma,j}$ and $\omega_{\alpha,j}$, with the ones in Myra *et al.* [37], in physical units. For an easier comparison we express our results also in physical units. We note that with the hypothesis of $\tilde{L}_1=\tilde{L}_2$ and $\tilde{n}_1=\tilde{n}_2$, our frequencies expressions in physical units reduce to the large aspect ratio limit of the ones derived in Ref. [37]. For ω_σ, we use the relation $\nu=e^2n_0R_0/(m_i\sigma_\parallel c_{s0})$.

Dividing eq. (51) by $\gamma_{\rm mhd}^2$, we obtain

$$1+\hat{\omega}^2+\frac{i\hat{\omega}\Theta(\hat{\omega}+i\varepsilon_\chi^2\Theta)}{\Lambda(\hat{\omega}+i\varepsilon_\chi^2\Theta)+i\varepsilon_\chi^2\frac{\omega_{\sigma,2}}{\omega_{\sigma,1}}\Theta}=0 \tag{52}$$

where the normalised frequency $\hat{\omega}=\omega/\gamma_{\rm mhd}$ is introduced, as well as the parameters that mostly affect the blob motion, i.e. $\Theta=\omega_{\alpha,1}/\gamma_{\rm mhd}$ and $\Lambda=\omega_{\alpha,1}/\omega_{\sigma,1}$. The Θ and Λ parameters describe, respectively, the importance of the sheath resistivity with respect to the interchange

	Our model (dimensionless units)	Our Model (physical units)	Myra *et al.* [37] (physical units)
γ^2_{mhd}	$-2\rho_s^2 \frac{R_0}{\rho_{s0}} \frac{1}{n_{0,1}} \frac{\partial n_1}{\partial x}$	$-2\frac{\Omega_0^2 \tilde{\rho}_s^2}{R_0} \frac{1}{\tilde{n}_{0,1}} \frac{\partial \tilde{n}_1}{\partial \tilde{x}}$	$-2\frac{\tilde{\Omega}^2 \tilde{\rho}_s^2}{\tilde{R}} \partial_{\tilde{x}} \ln n_1$
$\omega_{\sigma,j}$	$\left(\nu L_1 L_j n_{0,j} k_1^2\right)^{-1}$	$\frac{\Omega_0^2 m_i \sigma_\parallel}{e^2 \tilde{L}_1 \tilde{L}_j \tilde{n}_{0,j} \tilde{k}_1^2}$	$\frac{\tilde{\Omega}^2 m_i \sigma_\parallel}{e^2 \tilde{L}_\parallel^2 \tilde{n}_1 \tilde{k}_1^2}$
$\omega_{\alpha,j}$	$\left(\rho_s L_2 k_j^2\right)^{-1}$	$\frac{\Omega_0}{\tilde{\rho}_s \tilde{L}_2 \tilde{k}_j^2}$	$\frac{2\tilde{\Omega}}{\tilde{\rho}_s \tilde{L}_\parallel \tilde{k}_j^2}$

Table 1: Comparison of the characteristic frequencies of the two-region model as derived in the present work and as derived by Myra *et al.* [37]. In the first column the dimensionless frequencies are written in GBS dimensionless units, the second column translates them in physical units and, finally, the third column reproduces the expressions from the referenced article. The physical expression $\omega_{\sigma,j}$ are evaluated imposing $\nu = e^2 n_0 R_0/(m_i \sigma_\parallel c_{s0})$, with $\sigma_\parallel$ parallel conductivity.

drive and with respect to the plasma resistivity. Let us estimate the values of Λ and Θ as functions the blob properties

$$\Lambda = \frac{n_1 \alpha}{\sigma_1} = \frac{\omega_{\alpha,1}}{\omega_{\sigma,1}} = \nu n_1 \frac{L_1^2}{L_2 \rho_s} \tag{53}$$

$$\Theta = \frac{\omega_{\alpha,1}}{\gamma_{\text{mhd}}} = \left[\frac{k_1^{-4} a_x}{2\rho_s^4 L_2^2 \frac{\Delta_x n_1}{n_{0,1}} \rho_*^{-1}} \right]^{\frac{1}{2}} \overset{\text{fig 9}}{=} \left[\frac{(2a_y/\pi)^{\frac{4}{5}} a_x^{\frac{1}{5}}}{\left(2\rho_s^4 L_2^2 \frac{\Delta_x n_1}{n_{0,1}} \rho_*^{-1}\right)^{\frac{1}{5}}} \right]^{\frac{5}{2}} = \left(\frac{a_b}{a^*}\right)^{\frac{5}{2}} = \hat{a}^{\frac{5}{2}} \tag{54}$$

Here $\Delta_x n_1$ is an estimate of the variation of the blob density in x, such that $\partial_x n_1$ can be approximated with $\Delta_x n_1 / a_x$, where a_x represents the blob radius in the radial direction. In the general case of background density varying in x over the blob extension, $\Delta_x n_1 \neq \delta n_1$ and a_x, is half of the radial extension of the entire perturbation above background. In addition, $a_b = (2a_y/\pi)^{4/5} a_x^{1/5}$ is used to estimate of the blob size, while a^* is the reference size, which is given by the balance between the curvature drive β and the sheath current α (defined in eq. (38)):

$$a^* = \left(2\rho_s^4 L_2^2 \frac{\Delta_x n_1}{n_{0,1}} \rho_*^{-1}\right)^{\frac{1}{5}} = \left(\frac{\beta}{\alpha^2} \frac{\Delta_x n_1}{n_{0,1}} \rho_*^{-1}\right)^{\frac{1}{5}} \tag{55}$$

We now derive an analytical prediction for the blob radial velocity, as a function of the normalised blob size $\hat{a}$ (or Θ) and the collisionality Λ. As a first step, we express the radial velocity v_x as a function of the frequency ω. Since the radial blob motion is due to the $\mathbf{E} \times \mathbf{B}$ drift, using the linearised continuity equation (43), one can write:

$$v_x = v_E = \text{Im}(\omega) \frac{\rho_{s0}}{R_0} \frac{\delta n_1}{\Delta_x n_1} a_x \tag{56}$$

as $\partial_x n_1 = \Delta_x n_1 / a_x$, and $v_E = -ik_1 \delta\phi_1$. The reference velocity v^* is chosen such that the normalised velocity, $\hat{v} = v_x / v^*$, reads

$$\hat{v} = \text{Im}(\hat{\omega}) \hat{a}^{1/2} \tag{57}$$

By using equations (56) and (57) the reference velocity reads:

$$v^* = \frac{v_x}{\text{Im}(\hat{\omega}) \hat{a}^{-1/2}} = \gamma_{\text{mhd}} \frac{\rho_{s0}}{R_0} \frac{\delta n_1}{\Delta_x n_1} a_x \hat{a}^{-1/2} = \rho_s \left[8 \frac{\delta n_1^5}{\Delta_x n_1^2 n_{0,1}^3} \left(\frac{\pi a_x}{2a_y}\right)^2 \rho_s^2 L_2 \rho_*^2 \right]^{\frac{1}{5}} \tag{58}$$

We note that the chosen reference velocity can be interpreted as the radial velocity of a blob of size $\hat{a} = 1$, when the Resistive Balooning is the dominant instability, for which the drive in region 1 is balanced by the inertia in the same region (i.e. the first and last terms in eq. (48)) and $\omega_{\text{RB}} = i\gamma_{\text{mhd}}$.

In the high collisionality case $\Lambda \gg 1$, of interest in the present paper, one can incur either in the RB, if $\Lambda \gg \Theta$, or in the RX regime, if $\Lambda \ll \Theta$. Since $\Lambda \gg 1$, then $\omega_\alpha \gg \omega_\sigma$, and the linearised vorticity equation in region 2 (see eq. (49)) reduces to

$$\omega \simeq i\omega_{\sigma,2} \frac{\delta\phi_1}{\delta\phi_2} - i\omega_{\alpha,2} \tag{59}$$

	Our model (dimensionless units)	Our Model (physical units)	Myra *et al.* [37] (physical units)
Λ	$\nu n_1 \frac{L_1^2}{L_2 \rho_s}$	$\frac{\nu_1^{e/i} \tilde{L}_1^2}{\tilde{\rho}_s \Omega_{0,e} \tilde{L}_2}$	$\frac{\nu_1^{e/i} \tilde{L}_\parallel}{\tilde{\rho}_s \tilde{\Omega}_e}$
a_b	$\left(\frac{2a_y}{\pi}\right)^{\frac{4}{5}} a_x^{\frac{1}{5}}$	$\left(\frac{2\tilde{a}_y}{\pi}\right)^{\frac{4}{5}} \tilde{a}_x^{\frac{1}{5}}$	$\tilde{a}_b$
a^*	$\left(2\rho_s^4 L_2^2 \frac{\Delta_x n_1}{n_{0,1}} \frac{R_0}{\rho_{s0}}\right)^{\frac{1}{5}}$	$\tilde{\rho}_s \left[\frac{2\tilde{L}_2^2}{\tilde{\rho}_s R_0} \frac{\Delta_x \tilde{n}_1}{\tilde{n}_{0,1}}\right]^{\frac{1}{5}}$	$\tilde{\rho}_s \left[\frac{\tilde{L}_\parallel^2}{\tilde{\rho}_s \tilde{R}}\right]^{\frac{1}{5}}$
v^*	$\rho_s \left[8C(n_1)\rho_s^2 L_2 \frac{\rho_{s0}^2}{R_0^2}\right]^{\frac{1}{5}}$	$\tilde{c}_s \left(8C(n_1)\frac{\tilde{\rho}_s^2 \tilde{L}_2}{R_0^3}\right)^{\frac{1}{5}}$	$\tilde{c}_s \left(\frac{\tilde{\rho}_s^2 \tilde{L}_\parallel}{\tilde{R}^3}\right)^{\frac{1}{5}}$

Table 2: Comparison of main blob parameters expression as derived here and as reported in the reference article [37]. Columns 1 and 2 contain the same expressions in GBS units and in physical units respectively. Myra's expression in physical units are reported in the third column. In v^*, $C(n) = (\delta n_1^5 / \Delta_x n_1^2 n_{0,1}^3)(\pi a_x/(2a_y))^2$.

Since $\omega_{\sigma,2}$ is small relatively to $\omega_{\alpha,2}$, either the parallel current term $i\omega_{\sigma,2}\delta\phi_1/\delta\phi_2$ drops completely or, alternatively $\delta\phi_1 \gg \delta\phi_2$. In the first case the two regions are completely disconnected and the perturbation does not extend to region 2, therefore $\delta\phi_2 \sim 0$ and, in region 1, the inertia balances the drive (RB regime), from eq. (48):

$$\omega^2\delta\phi_1 = -\gamma_{\text{mhd}}^2\delta\phi_1, \tag{60}$$

this leads to $\hat{\omega}_{\text{RB}} = i$ and $\hat{v}_{\text{RB}} = \hat{a}^{\frac{1}{2}}$ [43] [44]. On the other hand, if $\delta\phi_1 \gg \delta\phi_2$ (RX regime), in region 1

$$\omega^2 = -i\omega_{\sigma,1}\omega - \gamma_{\text{mhd}}^2 \tag{61}$$

i.e., the parallel current balances the interchange drive:

$$\hat{\omega}_{\text{RX}} = i\frac{\gamma_{\text{mhd}}}{\omega_{\sigma,1}} = i\frac{\Lambda}{\Theta}, \tag{62}$$

and $\hat{v}_{\text{RX}} = \Lambda\hat{a}^{-2}$. The transition threshold between the two regimes is at $\Theta = \Lambda$, as it can be observed in eq. (61):

$$\hat{\omega}^2 + i\frac{\Theta}{\Lambda}\hat{\omega} + 1 = 0 \tag{63}$$

If $\Lambda > \Theta$ (RB regime) first and third term balance, alternatively, if $\Lambda < \Theta$ the second and the third term balance (RX regime), and the first term drops since $|\hat{\omega}^2| = (\Lambda/\Theta)^2 \ll 1$. The same result for these two regimes can be obtained more formally, but less intuitively, by taking the limit of the dispersion relation in eq. (52) for high values of Λ and obtaining directly the above eq. (63).

References

[1] D. D'Ippolito, J. Myra, and S. Zweben, "Convective transport by intermittent blob-filaments: Comparison of theory and experiment," *Physics of Plasmas*, vol. 18, no. 6, p. 060501, 2011.

[2] S. Zweben, "Search for coherent structure within tokamak plasma turbulence," *The Physics of fluids*, vol. 28, no. 3, pp. 974–982, 1985.

[3] J. Terry, S. Zweben, K. Hallatschek, B. LaBombard, R. Maqueda, B. Bai, C. Boswell, M. Greenwald, D. Kopon, W. Nevins, *et al.*, "Observations of the turbulence in the scrape-off-layer of alcator c-mod and comparisons with simulation," *Physics of Plasmas*, vol. 10, no. 5, pp. 1739–1747, 2003.

[4] B. Goncalves, C. Hidalgo, C. Silva, M. Pedrosa, and K. Erents, "Statistical description of the radial structure of turbulence in the jet plasma boundary region," *Journal of nuclear materials*, vol. 337, pp. 376–380, 2005.

[5] H. Tanaka, N. Ohno, N. Asakura, Y. Tsuji, H. Kawashima, S. Takamura, Y. Uesugi, *et al.*, "Statistical analysis of fluctuation characteristics at high-and low-field sides in l-mode sol plasmas of jt-60u," *Nuclear Fusion*, vol. 49, no. 6, p. 065017, 2009.

[6] N. Fedorczak, J. P. Gunn, P. Ghendrih, P. Monier-Garbet, and A. Pocheau, "Flow generation and intermittent transport in the scrape-off-layer of the tore supra tokamak," *Journal of Nuclear Materials*, vol. 390, pp. 368–371, 2009.

[7] O. E. Garcia, J. Horacek, R. Pitts, A. H. Nielsen, W. Fundamenski, V. Naulin, and J. J. Rasmussen, "Fluctuations and transport in the tcv scrape-off layer," *Nuclear fusion*, vol. 47, no. 7, p. 667, 2007.

[8] U. Pfeiffer, M. Endler, J. Bleuel, H. Niedermeyer, and G. Theimer, "Density, temperature and potential fluctuation measurements with multiple fast swept langmuir probes on w7-as," *Contributions to Plasma Physics*, vol. 38, no. S1, pp. 134–144, 1998.

[9] T. Happel, F. Greiner, N. Mahdizadeh, B. Nold, M. Ramisch, and U. Stroth, "Generation of intermittent turbulent events at the transition from closed to open field lines in a toroidal plasma," *Physical review letters*, vol. 102, no. 25, p. 255001, 2009.

[10] N. Vianello, M. Spolaore, M. Agostini, R. Cavazzana, G. De Masi, E. Martines, B. Momo, P. Scarin, S. Spagnolo, and M. Zuin, "On the statistics and features of turbulent structures in rfx-mod," *Plasma Physics and Controlled Fusion*, vol. 58, no. 4, p. 044009, 2016.

[11] D. Pace, M. Shi, J. Maggs, G. Morales, and T. Carter, "Exponential frequency spectrum and lorentzian pulses in magnetized plasmas," *Physics of Plasmas*, vol. 15, no. 12, p. 122304, 2008.

[12] I. Furno, B. Labit, M. Podestà, A. Fasoli, S. Müller, F. Poli, P. Ricci, C. Theiler, S. Brunner, A. Diallo, *et al.*, "Experimental observation of the blob-generation mechanism from interchange waves in a plasma," *Physical review letters*, vol. 100, no. 5, p. 055004, 2008.

[13] S. Krasheninnikov, D. D'ippolito, and J. Myra, "Recent theoretical progress in understanding coherent structures in edge and sol turbulence," *Journal of Plasma Physics*, vol. 74, no. 5, pp. 679–717, 2008.

[14] I. P. E. G. on Divertor, I. P. E. G. on Divertor Modelling, Database, and I. P. B. Editors, "Chapter 4: Power and particle control," *Nuclear Fusion*, vol. 39, no. 12, p. 2391, 1999.

[15] D. Carralero, P. Manz, L. Aho-Mantila, G. Birkenmeier, M. Brix, M. Groth, H. Müller, U. Stroth, N. Vianello, E. Wolfrum, *et al.*, "Experimental validation of a filament transport model in turbulent magnetized plasmas," *Physical review letters*, vol. 115, no. 21, p. 215002, 2015.

[16] G. Xu, V. Naulin, W. Fundamenski, C. Hidalgo, J. Alonso, C. Silva, B. Goncalves, A. H. Nielsen, J. J. Rasmussen, S. Krasheninnikov, *et al.*, "Blob/hole formation and zonal-flow generation in the edge plasma of the jet tokamak," *Nuclear Fusion*, vol. 49, no. 9, p. 092002, 2009.

[17] N. Bisai, A. Das, S. Deshpande, R. Jha, P. Kaw, A. Sen, and R. Singh, "Edge and scrape-off layer tokamak plasma turbulence simulation using two-field fluid model," *Physics of plasmas*, vol. 12, no. 7, p. 072520, 2005.

[18] C. Theiler, I. Furno, P. Ricci, A. Fasoli, B. Labit, S. Müller, and G. Plyushchev, "Cross-field motion of plasma blobs in an open magnetic field line configuration," *Physical review letters*, vol. 103, no. 6, p. 065001, 2009.

[19] F. Avino, A. Fasoli, I. Furno, P. Ricci, and C. Theiler, "X-point effect on plasma blob dynamics," *Physical review letters*, vol. 116, no. 10, p. 105001, 2016.

[20] C. Tsui, J. Boedo, J. Myra, B. Duval, B. Labit, C. Theiler, N. Vianello, W. Vijvers, H. Reimerdes, S. Coda, *et al.*, "Filamentary velocity scaling validation in the tcv tokamak," *Physics of Plasmas*, vol. 25, no. 7, p. 072506, 2018.

[21] F. Riva, C. Colin, J. Denis, L. Easy, I. Furno, J. Madsen, F. Militello, V. Naulin, A. H. Nielsen, J. M. B. Olsen, *et al.*, "Blob dynamics in the torpex experiment: a multi-code validation," *Plasma Physics and Controlled Fusion*, vol. 58, no. 4, p. 044005, 2016.

[22] F. Militello, P. Tamain, W. Fundamenski, A. Kirk, V. Naulin, A. H. Nielsen, *et al.*, "Experimental and numerical characterization of the turbulence in the scrape-off layer of mast," *Plasma Physics and Controlled Fusion*, vol. 55, no. 2, p. 025005, 2013.

[23] J. R. Angus and M. V. Umansky, "Modeling of large amplitude plasma blobs in three-dimensions," *Physics of Plasmas*, vol. 21, no. 1, p. 012514, 2014.

[24] F. D. Halpern, A. Cardellini, P. Ricci, S. Jolliet, J. Loizu, and A. Mosetto, "Three-dimensional simulations of blob dynamics in a simple magnetized torus," *Physics of Plasmas*, vol. 21, no. 2, p. 022305, 2014.

[25] F. Nespoli, I. Furno, B. Labit, P. Ricci, F. Avino, F. Halpern, F. Musil, and F. Riva, "Blob properties in full-turbulence simulations of the tcv scrape-off layer," *Plasma Physics and Controlled Fusion*, vol. 59, no. 5, p. 055009, 2017.

[26] B. W. Shanahan and B. D. Dudson, "Blob dynamics in torpex poloidal null configurations," *Plasma Physics and Controlled Fusion*, vol. 58, no. 12, p. 125003, 2016.

[27] B. Dudson, A. Allen, G. Breyiannis, E. Brugger, J. Buchanan, L. Easy, S. Farley, I. Joseph, M. Kim, A. McGann, *et al.*, "Bout++: Recent and current developments," *Journal of Plasma Physics*, vol. 81, no. 1, 2015.

[28] N. Nace, P. Tamain, C. Baudoin, H. Bufferand, G. Ciraolo, N. Fedorczak, D. Galassi, P. Ghendrih, and E. Serre, "Impact of safety factor and magnetic shear profiles on edge turbulence in circular limited geometry," *Contributions to Plasma Physics*, 2018.

[29] W. Gracias, P. Tamain, E. Serre, R. Pitts, and L. Garcia, "The impact of magnetic shear on the dynamics of a seeded 3d filament in slab geometry," *Nuclear Materials and Energy*, vol. 12, pp. 798–807, 2017.

[30] R. Churchill, C. Chang, S. Ku, and J. Dominski, "Pedestal and edge electrostatic turbulence characteristics from an xgc1 gyrokinetic simulation," *Plasma Physics and Controlled Fusion*, vol. 59, no. 10, p. 105014, 2017.

[31] P. Ricci, F. Halpern, S. Jolliet, J. Loizu, A. Mosetto, A. Fasoli, I. Furno, and C. Theiler, "Simulation of plasma turbulence in scrape-off layer conditions: the gbs code, simulation results and code validation," *Plasma Physics and Controlled Fusion*, vol. 54, no. 12, p. 124047, 2012.

[32] F. Halpern, P. Ricci, S. Jolliet, J. Loizu, J. Morales, A. Mosetto, F. Musil, F. Riva, T. Tran, and C. Wersal, "The {GBS} code for tokamak scrape-off layer simulations," *Journal of Computational Physics*, vol. 315, pp. 388 – 408, 2016.

[33] P. Paruta, P. Ricci, F. Riva, C. Wersal, C. Beadle, and B. Frei, "Simulation of plasma turbulence in the periphery of diverted tokamak by using the gbs code," *Physics of Plasmas*, 2018. Accepted.

[34] S. I. Braginskii, "Transport Processes in a Plasma," *Reviews of Plasma Physics*, vol. 1, p. 205, 1965.

[35] A. Zeiler, J. F. Drake, and B. Rogers, "Nonlinear reduced braginskii equations with ion thermal dynamics in toroidal plasma," *Physics of Plasmas*, vol. 4, no. 6, pp. 2134–2138, 1997.

[36] F. D. Halpern, P. Ricci, B. Labit, I. Furno, S. Jolliet, J. Loizu, A. Mosetto, G. Arnoux, J. Gunn, J. Horacek, *et al.*, "Theory-based scaling of the sol width in circular limited tokamak plasmas," *Nuclear Fusion*, vol. 53, no. 12, p. 122001, 2013.

[37] J. Myra, D. Russell, and D. D'Ippolito, "Collisionality and magnetic geometry effects on tokamak edge turbulent transport. i. a two-region model with application to blobs," *Physics of plasmas*, vol. 13, no. 11, p. 112502, 2006.

[38] D. Carralero, M. Siccinio, M. Komm, S. Artene, F. D'Isa, J. Adamek, L. Aho-Mantila, G. Birkenmeier, M. Brix, G. Fuchert, *et al.*, "Recent progress towards a quantitative description of filamentary sol transport," *Nuclear Fusion*, vol. 57, no. 5, p. 056044, 2017.

[39] L. Easy, F. Militello, J. Omotani, N. Walkden, and B. Dudson, "Investigation of the effect of resistivity on scrape off layer filaments using three-dimensional simulations," *Physics of Plasmas*, vol. 23, no. 1, p. 012512, 2016.

[40] S. I. Krasheninnikov, "On scrape off layer plasma transport," *Physics Letters A*, vol. 283, no. 5-6, pp. 368–370, 2001.

[41] J. Loizu, P. Ricci, F. D. Halpern, and S. Jolliet, "Boundary conditions for plasma fluid models at the magnetic presheath entrance," *Physics of Plasmas*, vol. 19, no. 12, p. 122307, 2012.

[42] C. Theiler, I. Furno, A. Fasoli, P. Ricci, B. Labit, and D. Iraji, "Blob motion and control in simple magnetized plasmas," *Physics of Plasmas*, vol. 18, no. 5, p. 055901, 2011.

[43] O. Garcia, N. Bian, V. Naulin, A. Nielsen, and J. J. Rasmussen, "Mechanism and scaling for convection of isolated structures in nonuniformly magnetized plasmas," *Physics of Plasmas*, vol. 12, no. 9, p. 090701, 2005.

[44] J. Myra and D. D'Ippolito, "Edge instability regimes with applications to blob transport and the quasicoherent mode," *Physics of Plasmas*, vol. 12, no. 9, p. 092511, 2005.